Static coded illumination strategies for low-dose x-ray material decomposition

ANGELA P. CUADROS,[1] CARLOS M. RESTREPO,[1] PETER NOËL,[2] AND GONZALO R. ARCE[1,*]

[1]*Department of Electrical and Computer Engineering, University of Delaware, Newark, Delaware 19716, USA*
[2]*Department of Radiology, Perelman School of Medicine, University of Pennsylvania, Philadelphia, Pennsylvania 19104, USA*
*Corresponding author: arce@udel.edu

Static coded aperture x-ray tomography was introduced recently where a static illumination pattern is used to interrogate an object with a low radiation dose, from which an accurate 3D reconstruction of the object can be attained computationally. Rather than continuously switching the pattern of illumination with each view angle, as traditionally done, static code computed tomography (CT) places a single pattern for all views. The advantages are many, including the feasibility of practical implementation. This paper generalizes this powerful framework to develop single-scan dual-energy coded aperture spectral tomography that enables material characterization at a significantly reduced exposure level. Two sensing strategies are explored: rapid kV switching with a single-static block/unblock coded aperture, and coded apertures with non-uniform thickness. Both systems rely on coded illumination with a plurality of x-ray spectra created by kV switching or 3D coded apertures. The structured x-ray illumination is projected through the objects of interest and measured with standard x-ray energy integrating detectors. Then, based on the tensor representation of projection data, we develop an algorithm to estimate a full set of synthesized measurements that can be used with standard reconstruction algorithms to accurately recover the object in each energy channel. Simulation and experimental results demonstrate the effectiveness of the proposed cost-effective solution to attain material characterization in low-dose dual-energy CT. © 2022 Optica Publishing Group

1. INTRODUCTION

Recently, several health problems have been associated with the high exposure to x-ray radiation. Thus, given the concern for the rapid increase in radiation dose by the expanded use of computed tomography (CT), multiple research groups have led major efforts to develop new approaches to reduce radiation dosage while maintaining acceptable image quality [1,2]. Multiple approaches used to attain this goal result in a set of incomplete measurements compared to the conventional number of sampling points needed for reconstruction [3]. Incomplete measurements in x-ray transmission CT have been a topic of study for many years in the context of limited angle tomography, where the number of views is reduced considerably [4]. Yet, as demonstrated by multiple research groups, using structured illumination to subsample the detectors instead of the number of angles results in higher quality reconstructions [5]. New approaches to further reduce radiation dose in conventional CT have been considered recently [1]. Dynamic fluence field modulation, for instance, was proposed to adaptively shape the beam during the CT scan, which can reduce radiation dosage [6]. Another type of modulation is to directly obtain sparse data instead of shaping the beam. Multiple

research groups have investigated sparse data acquisition by reducing the number of view angles at which projections are taken. However, given that compressive sensing algorithms are usually used to perform reconstructions, further randomization is desired across more directions. Chen *et al.* proposed the use of a multi-slit collimator placed in front of the x-ray source that moves axially to attain sparse data across the detector and introduces randomization across view angles, a system denominated SparseCT [7,8]. More recently, Rezaeian *et al.* expanded this idea using a 2D sparse grid structure, denominated Sparse Blockers, which continuously moves parallel to the detector allowing sparse data acquisition as well as scattering estimation and correction [9]. We recently introduced a low-dose CT system coined "StaticCode CT" that overcomes possible hardware limitations that arise by the continuous movement of the collimator or filter, by using a single-static coded aperture (CA) system paired with computational imaging algorithms to reduce 75% of radiation dosage [10]. The generalization of the aforementioned systems for dose reduction in multi-energy CT is of great interest in many applications. New and innovative ways of lowering the radiation dose in multi-energy x-ray systems is of particular interest in the medical diagnosis field.

To this end, this paper generalizes the StaticCode CT framework to the multi-energy domain. In particular, we aim at obtaining dual-energy reconstructions using low-dose transformations of currently available systems, thus providing a cost-effective solution to attain material decomposition. Figure 1 depicts possible implementations of the proposed coding solutions. Particularly, Fig. 1(A) depicts a dual-source system with a static block/un-block CA. In this system, there are two sources in two different trajectories, each one with a different kV potential and a different CA pattern. Then, the algorithm developed in [10] can be used to solve the inverse problem for each energy independently. Figure 1(B) depicts a rapid kV switching system with a CA. In this system, a single-static CA is placed in front of the x-ray source and the tube alternates between low- and high-energy potentials to attain dual-energy data. Figure 1(C) depicts a split filter system with a static CA. Each filter modifies the spectra to attain the energy data, while the CA is used to lower the radiation dose. Finally, Fig. 1(D) depicts the implementation of 3D CAs that by varying the thickness of a filter material attain a lower radiation dose while modifying the spectra. Without loss of generality, in this paper, we describe the process to attain dual-energy reconstructions using the systems shown in Fig. 1(B), rapid kV switching using a single-static CA, and 1D, 3D CAs.

The paper thus introduces a StaticCode CT approach for dual-energy architectures. The set of projection measurements embeds multi-energy attenuation characteristics of the subject to be used in image reconstruction. The strategy is further extended where the 2D CA is replaced by a static 3D CA that is carefully designed to block, unblock, and attenuate x rays to interrogate the volume of a subject. In this case, only a single-energy source CT scanner operating at a single kVp is needed to attain spectral CT measurements. Material decomposition reconstruction algorithms are presented based on novel tensor completion algorithms, and the evaluation of these methods in simulations with a water–iodine phantom are presented.
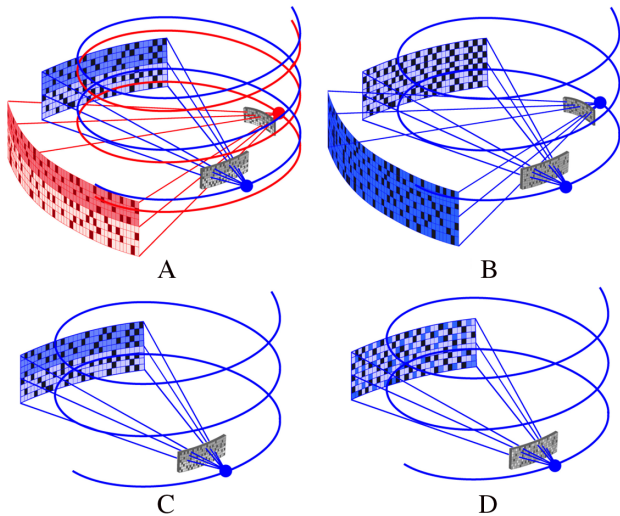

Fig. 1. Low-dose dual-energy with coded aperture implementations. (A) Dual-source system with a coded aperture. (B) Rapid kV switching with a coded aperture. (C) Split filters with a coded aperture. (D) Multidimensional coded aperture.

2. FORWARD MODEL

The forward model for StaticCode CT in dual-energy architectures is developed for a fan-beam x-ray CT system. However, the generalization to cone-beam CT and other 3D geometries is presented in Section 3. Given a line detector with Q elements, and an x-ray source that follows a circular trajectory around the object, the post-log data at the jth detector for the effective energy $\bar{E}$, defined as the energy of a monoenergetic source that would produce the same measurements as the poly-energetic source, are given by [11]

$$\mathbf{y}_j = \ln\left(I_{0j}(\bar{E})/I_j\right) = \int_\ell \mu(\ell, (\bar{E}))\mathrm{d}\ell, \qquad (1)$$

where $I_{0j}(\bar{E})$ is the x-ray photon intensity of the source, and $\mu(\ell, \bar{E})$ is the linear attenuation coefficient of the object at position ℓ and energy $\bar{E}$. After discretizing the system, the discrete-to-discrete formulation can be written as a finite linear system of equations of the form $\mathbf{y} = \mathbf{H}x$, where $\mathbf{H} \in \mathbb{R}^{QP \times N^2}$ is the system matrix, P is the number of view angles, and the $N \times N$ object has been vectorized, represented by $\mathbf{x}$. Multiple algorithms such as the FDK can then be used to obtain the effective linear attenuation coefficients of the object. However, in single-energy CT, materials having different compositions may be represented by the same gray-scale value. Hence, material differentiation can be very challenging.

Spectral CT relies on the energy and material dependence of x-ray linear attenuation coefficients. Namely, measurements obtained with different effective energies can be used to differentiate among multiple materials. Mathematically, basis material decomposition can be performed in the image domain as follows:

$$\mathbf{x}_i^c = \sum_{m=1}^{M} \mu_{mc} \rho_i^m, \qquad (2)$$

where $\mathbf{x}_i^c$ is the effective linear attenuation coefficient at pixel i and energy channel c, μ_{mc} is the effective mass attenuation coefficient of the mth basis material at the cth energy channel, and ρ_i^m is the mass density of material m at pixel i [12]. In dual-energy systems, two sets of data, one corresponding to a high-energy spectrum and a second one using a low-energy spectrum, are acquired. Then, (2) can be solved in a pixel-by-pixel basis to yield the mass densities for $M = 2$ materials using the reconstructions of the linear attenuation coefficients for each spectrum.

A. Rapid kV Switching Using a Single Coded Aperture

Figure 1(B) depicts the rapid kV switching CA system, which generalizes the system in [10] to dual-energy rapid kV switching. Here, a static block/unblock CA is placed in front of the x-ray source, and at every view angle, we switch the tube potential from high to low energy and vice versa to attain dual-energy data. As shown in [13], the acquired projections are an interleaved coded sinogram, where the linear attenuation coefficients for each energy channel can be obtained as follows:

$$\hat{\boldsymbol{x}}^c = \operatorname*{argmin}_{\mathbf{x}^c} \| \mathbf{y}^c - \mathbf{C}^c \mathbf{H} \mathbf{x}^c \|_2^2 + \lambda \| \mathbf{x}^c \|_p, \quad c = \{L, H\},$$

(3)

where λ is a regularization constant, c is the energy channel ($L =$ Low, $H =$ High), $\| \cdot \|_2$ corresponds to the ℓ_2 norm, and $\| \cdot \|_p$ represents any prior information about the data and the binary matrix, and $\mathbf{C}^c$ accounts for the kV switching as well as for the CA. As demonstrated in our previous work [14,15], CAs can be optimized to attain higher reconstruction quality. Furthermore, since a single CA is used in all view angles, some pixels in the center of the image are not sensed, and there are ring patterns in the sensing distribution that can produce artifacts in the axial reconstructions [10]. Thus, we use uniform sensing patterns in the CA and implement a tensor strategy to estimate the missing data based on the tensor representation of the measurements. Particularly, we recover the missing entries in the 3D tensor representation of the measurements using the ADMM algorithm developed in [16]. Given that a complete set of measurements is obtained for each energy channel, we can use conventional reconstruction algorithms to reconstruct the linear attenuation coefficients for each channel, which in turn can be used in (2) to attain material composition information for each pixel [13]. Mathematically, the material decomposition can be written as follows:

$$\begin{pmatrix} x_i^H \\ x_i^L \end{pmatrix} = \begin{pmatrix} \mu_{1H} & \mu_{2H} \\ \mu_{1L} & \mu_{2L} \end{pmatrix} \begin{pmatrix} \rho_i^1 \\ \rho_i^2 \end{pmatrix},$$

(4)

where ρ_i^m corresponds to the concentration of the mth basis material in the object at the ith pixel, and $\mu_{mH/L}$ is defined as the effective mass attenuation coefficient of each base material ($m = 1, 2$) measured at the corresponding energy spectrum. Then, as previously mentioned, the following matrix inversion can be performed to solve the inverse problem in a pixel-by-pixel basis:

$$\begin{pmatrix} \rho_i^1 \\ \rho_i^2 \end{pmatrix} = \frac{1}{\mu_{1H}\mu_{2L} - \mu_{2H}\mu_{1L}} \begin{pmatrix} \mu_{2L} & -\mu_{2H} \\ -\mu_{1L} & \mu_{1H} \end{pmatrix} \begin{pmatrix} x_i^H \\ x_i^L \end{pmatrix}.$$

(5)

Alternatively, we can use a constrained least-squares algorithm to solve for ρ_i^1 and ρ_i^2 for each pixel independently in (4), which is the approach taken in this paper.

B. Single Coded Aperture with Non-Uniform Thickness

In current implementations of fast-kV switching, independent pre-filtration of the spectrum for each energy is not feasible due to the short time between acquisitions, which hinders accurate energy separation. Thus, in this work, a CA with a non-uniform thickness is proposed as an alternative method to acquire dual-energy projections. To that end, the CA structure has multiple levels of thickness distributed across the mask, rather than the conventional block/unblock distribution used in single-energy CT. Figure 2 depicts an example of the proposed structure. In this case, three different thicknesses of tungsten are used to filter the x-ray beam. The un-filtered x-ray source spectrum is depicted in black, and the blue, red, and magenta spectra correspond to filtering 30%, 60%, and 95% of the x-ray flux, respectively. Note that the unfiltered and 30% x-ray beams generate relatively low-energy x-ray projection data, while the 60%, and 95% filtered beams make high-energy projection data.
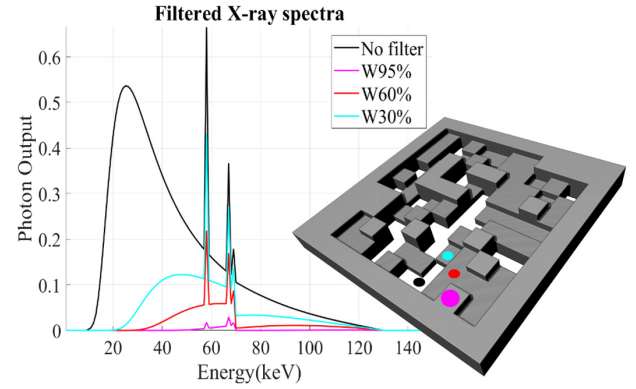

Fig. 2. Filtered spectra with tungsten (W) at different thicknesses and an example of the 3D coded aperture structure. The colors on the coded aperture structure indicate examples of the corresponding spectra.

Thus, rather than discarding the measurements corresponding to the filtered x rays, as in single-energy CT [10], the filtered data are used to attain spectral information from the object. Mathematically, taking into account the polychromatic nature of the x-ray beam, the filtered measurements at an integrating detector when using a filter f in front of the x-ray source are given by

$$I_j^f = \int_E I_0(E) \exp\left[-\mu_f(E)\delta_{j,f}\right] \exp\left(-\int_\ell \mu(\ell, E)\mathrm{d}\ell\right) \mathrm{d}E,$$

(6)

where $\mu_f(E)$ is the linear attenuation coefficient of the filter f at energy E, $I_0(E)$ is the x-ray source intensity at energy E, and $\delta_{j,f}$ is the length of the intersection of the jth x-ray beam with the filter f. The filter thickness of the CA can be designed such that the separation between low- and high energy spectra is maximum, which improves material characterization accuracy. It should be noted, however, that there is a trade-off between the separation of the spectra and the signal-to-noise ratio at the detector since in general heavy filtration will greatly impact the latter.

3. DUAL-ENERGY RECONSTRUCTION USING TENSOR COMPLETION

Here, we used the tensor completion framework developed in [10,13] to obtain a 3D tensor representation of the spectral projection data for both systems using a fan-beam architecture. In contrast to the monoenergetic case, the third dimension of the tensor corresponds to the number of available channels C. Namely, the projections' tensor is defined as $\mathcal{Y} \in \mathbb{R}^{Q \times P \times C}$. Figure 3(A) depicts the 3D tensor for a rapid kV switching dual-energy system using a single CA, obtained by stacking the $C = 2$ tiled subsampled sinograms corresponding to low and high energies, which correspond to the frontal slices of the tensor. Figure 3(B) depicts the 3D tensor for a conventional fan-beam CT system using a CA with multiple thicknesses. The frontal slices of the tensor, in the latter case, correspond to sinograms containing the measurements associated with a particular thickness. Thus, the CA pattern differs between channels, producing an alternating pattern. The fan-beam sinograms that make the frontal slices in both cases are gray-scale images with missing
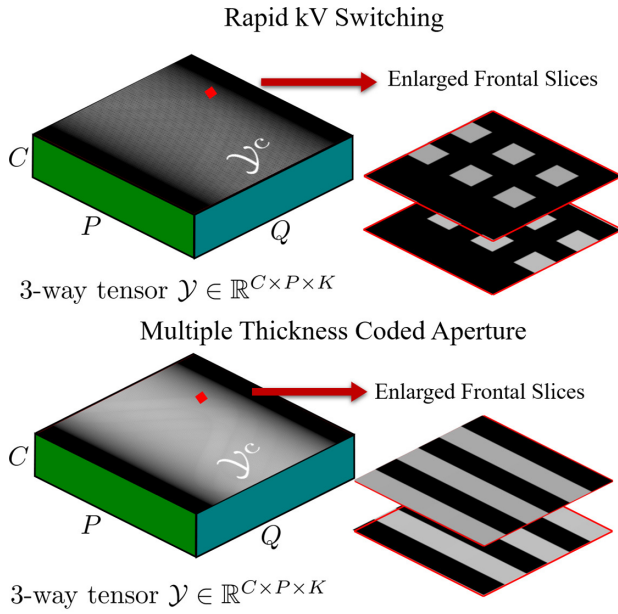
Rapid kV Switching

C P Q $\mathcal{Y}^c$

3-way tensor $\mathcal{Y} \in \mathbb{R}^{C \times P \times K}$

Enlarged Frontal Slices

Multiple Thickness Coded Aperture

C P Q $\mathcal{Y}^c$

3-way tensor $\mathcal{Y} \in \mathbb{R}^{C \times P \times K}$

Enlarged Frontal Slices

Fig. 3. Tensor representation of phantom projection data obtained (A) using a static coded aperture and kV switching and (B) using a static coded aperture with random thickness and a single kV.

patches that can be considered low rank. Furthermore, there is high correlation between the different energy channels since the spatial information remains largely unchanged. Therefore, we can exploit the multidimensional structure of the projections' tensor by estimating the missing measurements using the tensor completion framework developed in [10,17].

Namely, the measurement estimation problem is formulated as the following low-rank tensor completion model:

$$\hat{\mathcal{S}} = \underset{\mathcal{S}}{\arg\min} ||\mathcal{S}||_{\mathrm{TNN}} + \lambda \Phi(\mathcal{S}) \text{ s.t. } \mathcal{P}_\Omega(\mathcal{S}) = \mathcal{P}_\Omega(\mathcal{Y}), \quad \textbf{(7)}$$

where $\hat{\mathcal{S}}$ is the estimate of the projection data tensor, $\mathcal{Y}$ is the observed incomplete tensor, $\mathcal{P}_\Omega(\mathcal{Y}) = \mathcal{Y}(i, j, k)$ for $(i, j, k) \in \Omega$, otherwise $\mathcal{P}_\Omega(\mathcal{Y}) = 0$, and Ω is the set of indices associated with the unblocking CA elements. In the 3D CA case, Ω is constructed such that each of the frontal slices contains "missing measurements" in the positions where a different thickness is used. The data-driven regularization term $\Phi(\mathcal{S})$ is added to capture fine details in the reconstructed tensor that may not be well captured by the low-rank regularizer. Here, the ADMM framework developed in [16] is used to solve (7) and obtain an estimation of the measurement tensor. We used the simultaneous iterative reconstruction technique (SIRT) and FDK algorithms to reconstruct effective linear attenuation coefficients at each energy c using the corresponding estimated sinogram $\hat{\mathcal{S}}^c$, which is the cth frontal slice of the estimated measurement tensor. Nonetheless, other iterative or analytic reconstruction algorithms can be used as well.

A. Generalization to 3D Geometries

The material decomposition reconstruction algorithm remains unchanged for cone-beam CT. However, in the measurements' estimation process, an extra-dimension needs to be added to the

projection data tensor to account for the 2D detector. Consider a cone-beam CT scan of an object using a $Q_1 \times Q_2$ detector. Then, the set of measurements is arranged as a 4D tensor that can be represented as a vector of cubes for the multiple thickness CA system. Each cube represents a 3D tensor constructed by stacking the C subsampled FPD measurements at each view angle. The resulting tensor is represented mathematically as $\mathcal{Y} \in \mathbb{R}^{Q_1 \times Q_2 \times C \times P}$.

The low-rank tensor completion framework used to solve the inverse problem for the single-static CA system developed in [10], which integrates low rankness and the deep image prior, can be extended for higher-order tensors, as the one in multi-energy CT, by replacing the tensor nuclear norm (TNN) with its high-order extension, the weighted sum of TNN (WSTNN) [16]. The WSTNN is defined as

$$||\mathcal{Y}||_{\mathrm{WSTNN}} = \sum_{1 \le k_1 \le k_2 \le 4} \alpha_{k_1 k_2} ||\mathcal{Y}_{(k_1 k_2)}||, \quad \textbf{(8)}$$

where $\alpha_{k_1 k_2} > 0$, $\sum \alpha_{k_1 k_2} = 1$, and $\mathcal{Y}_{(k_1 k_2)}$ is the mode-$k_1 k_2$ tensor unfolding for $k_1 < k_2$. The mode-n matricization of a tensor $\mathcal{Y}_{(I_1 \times I_2 \times \cdots \times I_N)}$ is denoted by $\mathcal{Y}_{(n)}$ and arranges the mode-n fibers to be the columns of the resulting matrix. Recall that fibers are the higher-order analog of matrix rows and columns and are obtained by fixing every index of the tensor but one.

Then, the measurement estimation problem is formulated as follows:

$$\mathcal{S} = \underset{\mathcal{S}}{\arg\min} ||\mathcal{S}||_{\mathrm{WSTNN}} + \lambda \Phi(\mathcal{S}) \text{ s.t. } \mathcal{P}_\Omega(\mathcal{S}) = \mathcal{P}_\Omega(\mathcal{Y}). \quad \textbf{(9)}$$

Then the ADMM algorithm developed in [16] is used to solve the inverse problem. Note that the methods used to solve the inpainting are well suited for parallel computation on a GPU. Thus, the runtime is dominated by the algorithm used to solve the minimization of the WSTNN, which has complexity $O(N^3 \log N)$ [16].

4. SIMULATION RESULTS

The proposed approaches are tested to determine their capability of decomposing water and iodine using a 256×256 iodine sensitivity phantom, depicted in Figs. 4(A) and 4(B), with side length of 20 cm; it is composed of a water cylinder and a set of eight vials with varying iodine concentrations, namely, 4, 3, 2, 1, 0.75, 0.5, 0.25, and 0.1 mg/ml. The ASTRA tomography toolbox [18] is used to simulate a fan-beam x-ray CT configuration with a flat 1D detector strip composed of $Q = 1024$ elements of length 40 cm, and distances from the source to the center of rotation and the detector of 40 cm and 80 cm, respectively. The mass attenuation coefficients, for water and iodine, were obtained from the National Institute of Standards and Technology (NIST) x-ray attenuation databases available in [19], and the x-ray spectra were calculated using the Spektr software [20]. Figure 4(C) depicts the energy spectra simulated for low- and high-kVp tube potentials of the rapid kV switching system. The peaks were set to 80 and 140 kV and were modified by filtration with 2.0 mm of aluminum and 0.2 mm of copper. Peak kV was switched every projection. Figure 4(D) depicts the energy spectra simulated for a 140 kV peak x-ray source
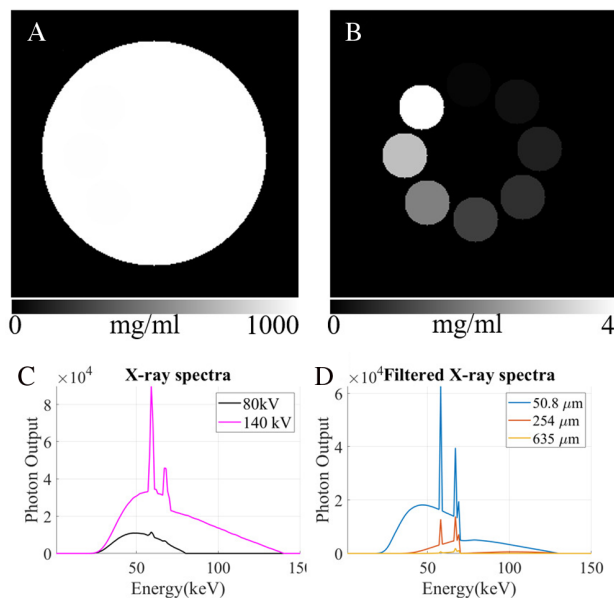
Fig. 4. (A) Water concentration, (B) iodine concentration, (C) dual kV switching spectra, and (D) tungsten filtered spectra.

modified by placing tungsten filters of different thicknesses to emulate the effect of the proposed 3D CA architecture. For this simulation scenario, we designed a CA with only two different thicknesses, namely, 50.8 µm and 254 µm. These two thicknesses were chosen taking into account the values of tungsten sheet thicknesses that can be acquired for implementation. To do a fair comparison of the systems, the energy of each spectrum was calculated, and the number of view angles was adjusted for three different scenarios: (I) rapid kV switching with a single CA of 37.7% transmittance, (II) multiple thickness CAs with 50% elements of each thickness, and (III) rapid kV switching with sparse view angles. In all scenarios, the radiation dosage was equivalent.

The multiple thickness CA was designed to alternate between the two thicknesses. In both systems, the CA mask was static with respect to the gantry. To attain equivalent energy, the rapid kV switching system was simulated to have a CA with a Bayer structure ([21]) with 37.5% transmittance, and it was used in a system with $P = 368$ view angles, while the 3D CA system had $P = 512$ view angles. Finally, the sparse view angle system with rapid kV switching had $P = 138$ view angles. Figures 5(A) and 5(B) depict the material decomposition results for the rapid kV switching with 37.5% transmittance CA, Figs. 5(C) and 5(D) depict the material decomposition results for the multiple thicknesses CA, and Figs. 5(E) and 5(F) depict the results for the sparse view angle system with rapid kV switching. Note that the rapid kV switching with sparse view angle reconstructions contains more noise than the proposed system's reconstructions. Furthermore, low concentrations of iodine are more discernible in the proposed method. In the three systems, SIRT is used to reconstruct the effective energy linear attenuation coefficients in each energy channel, then a constrained least-squares algorithm is used to solve the material decomposition problem for each pixel independently. Additionally, Fig. 6 depicts the concentration values for each system and for circular regions of interest (ROIs) centered in each of the iodine vials and with a radius
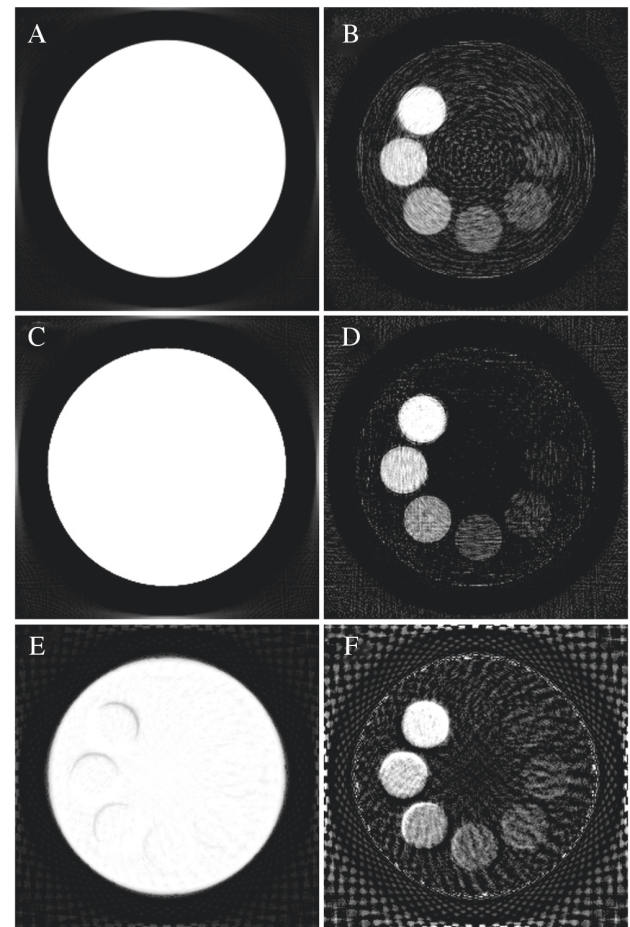

Fig. 5. Water–iodine material decomposition using SIRT reconstructions with 500 iterations for (A), (B) rapid kV switching with 37.5% transmittance coded aperture; (C), (D) multiple thicknesses coded aperture; and (E), (F) sparse angles and kV switching. Water concentration display is [0,1000] mg/ml, and iodine concentration display is [0,4] mg/ml.

equivalent to each vial. Note that the proposed method with the kV switching architecture gives the closest concentration values to the ground truth since the spectra are better suited for decomposition than those obtained with 3D CAs. Additionally, for comparison, Fig. 6 presents results obtained with the SIRT algorithm using only the observed rays rather than the proposed method for tensor completion to obtain a full set of rays. As can be seen, using the SIRT algorithm with the observed measurements compared to the proposed reconstruction method results in a greater error of concentration values for the kV switching architecture, and in the 3D CAs, the results are comparable. In our future research, we will look into improving the calibration method for the 3D CA method, since it shows great potential in preserving the proportionality of the concentration values.

A cone-beam CT configuration with a flat panel detector (FPD) with 660×660 elements with a 0.3880 mm pixel pitch and 360 projections in 1° increments was used in the subsequent simulations. The object consisted of multiple slices of the phantom used in Fig. 6 and simulates having vials of each material in a cylindrical phantom. After discretization, we obtain a $256 \times 256 \times 256$ data cube with 0.5 mm × 0.5 mm × 0.5 mm
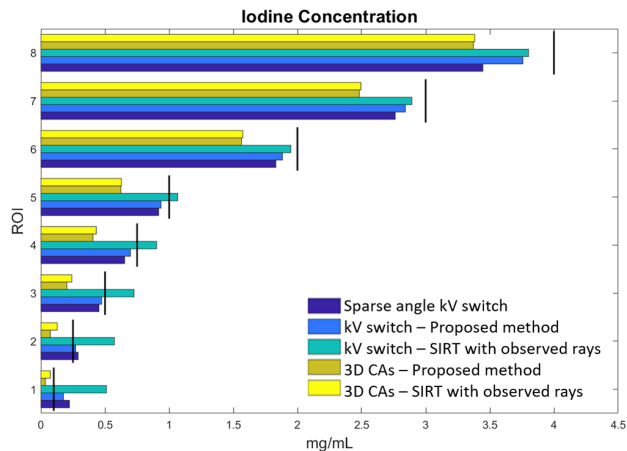
Fig. 6. Iodine concentration (mg/ml) for the proposed systems in each ROI. The black vertical lines denote the ground truth value in each ROI.

voxels. The distance from source to center was set to 60 cm, and the source to detector distance was set to 120 cm. The spectra used for this experiment are equivalent to those shown in Fig. 4(C); however, the bare-beam intensity was set to 10^6 photons per detector pixel. Last, Poisson noise and electronic noise (with 3.31 variance) were added to the projection data. A blue noise distribution was used to determine the position of the unblocking elements in the 35% transmittance CA, given that it has been demonstrated that using uniform sensing results in higher reconstruction quality [17,22,23]. To perform the reconstructions, we used the 4D tensor completion framework in (9) to estimate the missing measurements in the detector, and then we obtained the effective linear attenuation coefficients for
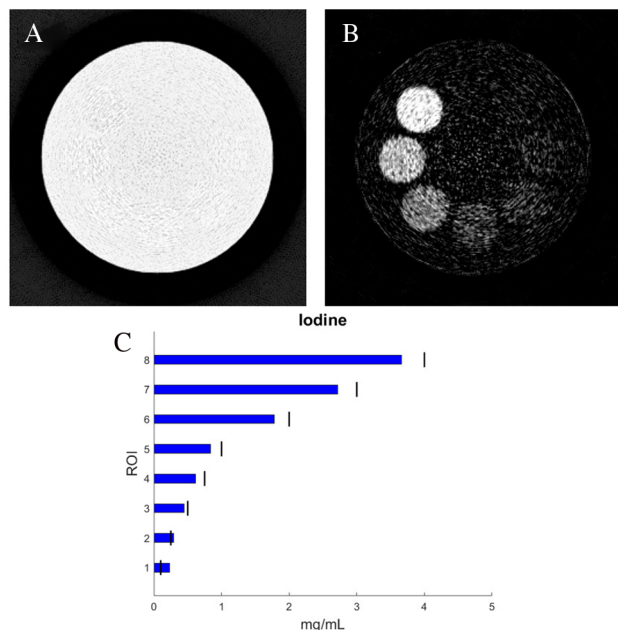

Fig. 7. (A), (B) Central axial slice of the water–iodine material decomposition reconstruction using SIRT with 500 iterations for rapid kV switching with a coded aperture with 37.5% transmittance for cone-beam projections. Water concentration display is [0,1000] mg/ml, and iodine concentration display is [0,4] mg/ml. (C) Iodine ROI concentration measure; black lines denote the ground truth.

high and low energies using the SIRT algorithm. Subsequently, we used a constrained least squares algorithm independently for each pixel in the volume to obtain the basis material decomposition. Figures 7(A) and 7(B) depict the material decomposition results for the central axial slice, and Fig. 7(C) depicts the iodine concentration in the ROIs. Note in the concentration figure that the reconstruction matches the expected concentrations for most of the vials, which demonstrates the effectiveness of the proposed approach to lower the radiation dosage while maintaining high accuracy in decomposition. Furthermore, it should be noted that the visual quality of the reconstructions can be improved by using iterative algorithms with a smoothing regularization if needed.

5. EXPERIMENTAL RESULTS

A Rigaku GX 130 CT Scanner located in the AMCL at the University of Delaware was used to experimentally demonstrate the results; Table 1 contains the hardware settings for the microCT scanner. The distances from the x-ray source to the center of rotation and the FPD were set to 120 mm and 224 mm, respectively, and the sample remained stationary while the gantry rotated around it in a circular trajectory. Due to hardware constraints, the mounting hardware for the CAs is located on the detector side as shown in Fig. 8. However, we have previously demonstrated that the system does not change if the CA is placed after the object and before the detector [24]. To determine the material differentiation capabilities of the proposed systems, the linearity plate of the X-ray micro-CT

Table 1.   Hardware Settings Used for Rigaku GX 130 CT

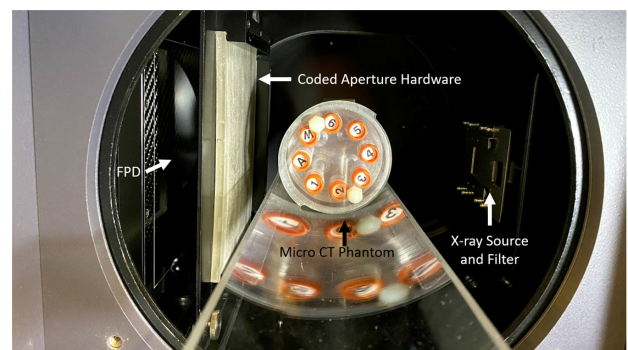| Setting	Value
X-ray focus (min)	5 μm
X-ray source to center of rotation	120 mm
FPD to center of rotation	224 mm
X-ray tube potential	130 kV
X-ray tube current	61 μA
FPD size	2352×2944 pixels
FPD detector element size	49.5 μm
Averaged frames	4
Total scanning time	2 min
Total number of frames	3308

Fig. 8. X-ray setup for kV switching with the CC576 coded aperture.

Phantom mCTP 610 was used [25]. The linearity plate consists of vials of varying iodine concentrations, namely, 0.9375, 1.875, 3.75, 7.5, 15, and 30 mg/ml. The 30 mg/ml solution was prepared by diluting 1.0 ml of full-strength nonionic iohexol contrast material (Omnipaque 300, GE Healthcare, Oakville, ON) with 9.0 ml of distilled water. Two additional vials of water and air were included, to facilitate calibration in HU. These eight vials were arranged in a concentric circle (44 mm diameter) and inserted into three polycarbonate plastic plates; each vial has an approximate diameter of 12.70 mm at the top. Binning is performed directly during the acquisition, therefore obtaining FPD measurements of 1136×1472 with a detector element size of 0.099 mm. For the kV switching experiment, the x-ray tube was operated at 130 kV and 100 µA for the high-energy scan, and 70 kV and 100 µA for the low-energy scan. In both cases, filters of aluminum and copper of 0.5 mm and 0.06 mm thicknesses, respectively, were used. Additionally, we designed a 3D printed plastic CA with pixel pitch 576 µm, hereinafter referred to as CC576. Cold casting was used to cast a tungsten epoxy resin composite (Technon Poly Kits [26]) onto the 3D printed structure to obtain a block/unblock blue noise pattern. The CC576 CA was placed in the Rigaku CT laboratory, and the previous cone-beam configuration was used to attain $P = 827$ projection measurements of the linearity plate of the microCT phantom. The setup is depicted in Fig. 8.

The kV switching data are obtained by selecting the even angles from the set of projections of the high-energy setup and the odd projections from the low-energy setup, and a calibration procedure to obtain the matrix of the mass attenuation coefficients of the base materials is performed prior to reconstruction.
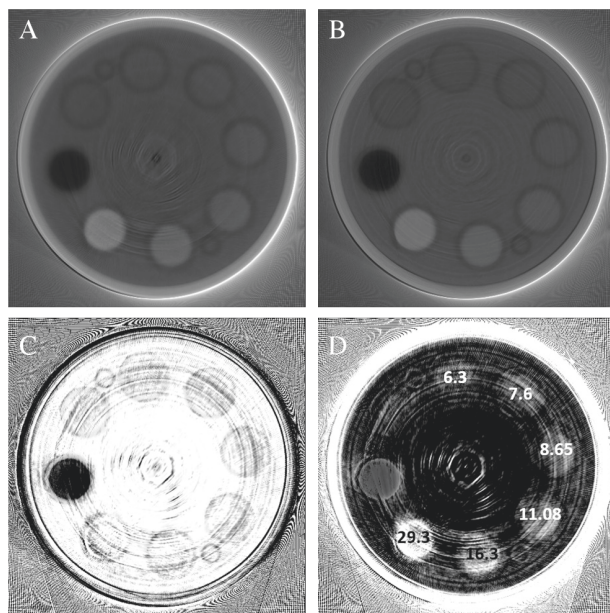
The coded projections are first inpainted using a matrix completion algorithm to attain a suitable initialization. Then, the estimated FPD measurements are stacked vertically for each energy channel, and the 4D tensor completion framework is used to obtain the complete tensor of dual-energy cone-beam measurements. Figures 9(A) and 9(B) depict the reconstructions for each energy channel, and the material decomposition corresponding to the 256th axial slice of the phantom obtained using the proposed measurement's estimation approach with the FDK algorithm is depicted in Figs. 9(C) and 9(D). The concentrations obtained for each vial are depicted in Fig. 9(D). As can be seen, the vials with the highest concentrations are
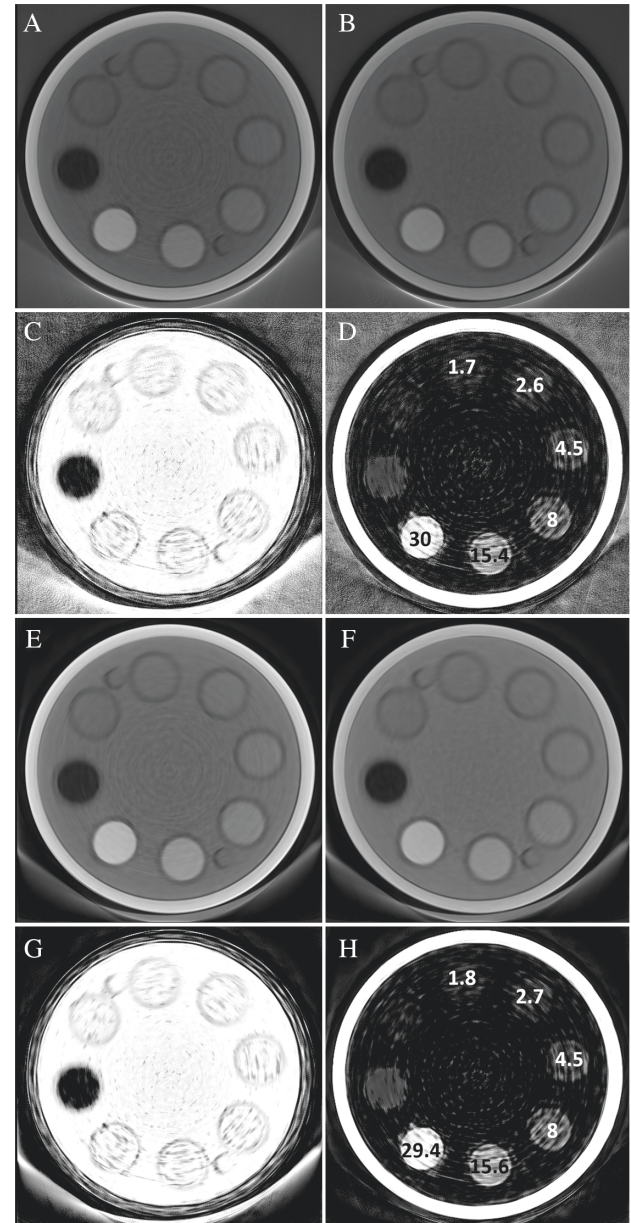

Fig. 9. kV switching with coded aperture cone-beam experimental reconstructions. (A), (B) FDK reconstructions of the 256th slice for 70 kV and 130 kV channels obtained from the estimated set of measurements. (C), (D) Water–iodine material decomposition for the 256th slice. Water concentration display is [0,1000] mg/ml, and iodine concentration display is [0,30] mg/ml. Iodine ROI concentration measures indicated in the center of each vial are given in mg/ml.

Fig. 10. kV switching with coded aperture fan-beam emulation. (A), (B) FBP reconstructions for 70 kV and 130 kV channels obtained from the estimated set of measurements. (C), (D) Water–iodine material decomposition. Water concentration display is [0,1000] mg/ml, and iodine concentration display is [0,30] mg/ml. Iodine ROI concentration measures indicated in the center of each vial are given in mg/ml. (E)–(H) Same results when using the SIRT algorithm.

accurately reconstructed with the proposed low-dose method. For this experiment, we do not include SIRT reconstructions, as the computational complexity of computing the reconstruction cannot be handled by the hardware resources available in the laboratory at the moment for a $512 \times 512 \times 512$ object.

As shown in Fig. 9, the reconstruction contains multiple ring artifacts that can be explained by the geometric magnification of CA elements on the FPD. To verify this statement, we perform an emulation of having one-to-one correspondence of CA elements with FPD elements, and we use the central rows of the FPD to attain a fan beam of the central axial slice using a 30% transmittance CA. Figures 10(A)–10(D) depict the reconstructions for each channel as well as the material decomposition using the FDK algorithm. Note that the artifacts are reduced in this experiment, and evidence that improving the CA manufacturing and correspondence with the FPD will result in improvements in the results. Figures 10(E)–10(H) depict reconstructions using the SIRT algorithm; as can be seen, both

algorithms perform similarly and are able to attain good material decomposition performance. Furthermore, as future work, the research group will experiment with varying the current as well as the integration time as means to reduce the noise in the proposed approaches while still attaining a lower radiation dose.

The final experiment aimed to emulate the performance of a 3D CA. In this case, the source was set to 130 kV and 120 μa. Additionally, two different tungsten thicknesses were used as filters in front of the x-ray source, namely, 0.0254 mm and 0.635 mm. The latter scan resulted in almost complete blockage of the source. To attain dual-energy data, an emulated CA consisted of unblocking elements, and elements with the aforementioned thicknesses. The number of elements for the unblocking elements and the 0.0254 mm thickness was the same, while the number of elements for the 0.635 mm thickness was set such that an equivalent amount of energy was attained when compared to the previous experiment. Figures 11(A)–11(D) depict the results for this experiment. As can be seen, the number of artifacts increases since the number of unblocking elements is very low. However, as previously mentioned, the optimization of the number of elements, as well as their distribution, is still an open problem that can improve the results greatly.

6. DISCUSSION AND CONCLUSION

Two low-dose x-ray dual-energy architectures based on StaticCode CT hardware principles are proposed and validated using a microCT scanner. The proposed systems enable imaging of an object with fewer measurements than most conventional systems and/or at a reduced exposure level, and they have the potential to provide a cost-effective alternative to photon counting spectral CT techniques and a faster scanning solution with a reduced x-ray radiation dose compared to traditional spectral CT imaging systems. Both systems rely on coded illumination with a plurality of x-ray spectra created by CAs. In the second system, the thicknesses and/or the materials used across the elements of the CA mask vary across the structure. In addition, as both systems use conventional integrating detectors, the spatial resolution that can be achieved is higher compared with photon counting detector systems in general. The methods developed in this paper can be directly applied to obtain material decomposition using other dual-energy scanners with CAs such as systems with a dual-source, dual-layer detector, and/or split-beam filtering.

As shown in Fig. 9, the reconstruction contains multiple ring artifacts that can be explained by the geometric magnification of CA elements on the FPD, which can be evidenced by the experiment results shown in Fig. 10 in which there is one to one correspondence of CA elements with detector elements. Furthermore, we plan to improve the calibration method for the material decomposition so that we can attain weights that correspond to the behavior of the materials under the scanner in use. Nonetheless, the ROI concentrations obtained are similar and in some cases outperform state-of-the-art systems for low-dose material decomposition [27]. Note that in this paper, we obtained object-free projections using the CA mask to obtain a mask array indicating the location of the measurements via thresholding segmentation [17]. However, advanced methods
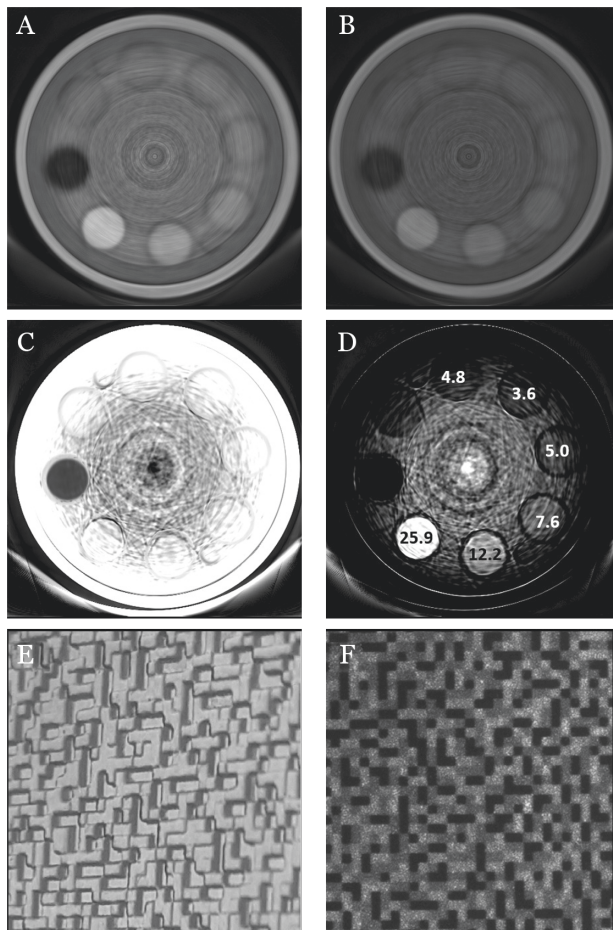

Fig. 11. 3D coded aperture fan-beam emulation. (A), (B) FBP reconstructions using a tungsten filter of 0.0254 mm and without a filter. Obtained from the estimated set of measurements. (C), (D) Water–iodine material decomposition. The concentrations are given in mg/ml. (E), (F) Possible manufacturing method for 3D coded apertures: (E) plastic mold and (F) radiograph after filling with tungsten/epoxy mixture. Water concentration display is [0,1000] mg/ml, and iodine concentration display is [0,30] mg/ml. Iodine ROI concentration measures indicated in the center of each vial are given in mg/ml.

to account for the "geometric" penumbra effect governed by the size and shape of the x-ray focal spot as well as the position of the CA are a topic of current research. Finally, Fig. 11 depicts a possible manufacturing method for the 3D CAs in future research. As can be seen, a 3D plastic mold with different thicknesses can be designed (Fig. 11(E)) such that when filled with the tungsten epoxy mixture, different energy profiles can be attained to perform material decomposition. Figure 11(F) depicts a radiograph obtained for a section of the 3D printed code after it was filled with the tungsten epoxy mixture. The calibration and implementation of this CA are topics of current work.

Disclosures. The authors declare no conflicts of interest.

Data Availability. The data underlying the results presented in Section 5 are available in Ref. [28]. A description of the data and how to use it can be found in Ref. [24]. The datasets are also available from the corresponding author upon reasonable request.

REFERENCES

1. J. Z. Liang, P. J. La Riviere, G. El Fakhri, S. J. Glick, and J. Siewerdsen, "Guest editorial low-dose CT: what has been done, and what challenges remain?" IEEE Trans. Med. Imaging **36**, 2409–2416 (2017).
2. C. H. McCollough, G. H. Chen, W. Kalender, S. Leng, E. Samei, K. Taguchi, G. Wang, L. Yu, and R. I. Pettigrew, "Achieving routine sub-millisievert CT scanning: report from the summit on management of radiation dose in CT," Radiology **264**, 567–580 (2012).
3. D. J. Brady, A. Mrozack, K. MacCabe, and P. Llull, "Compressive tomography," Adv. Opt. Photon. **7**, 756–813 (2015).
4. J. S. Jorgensen, E. Y. Sidky, and X. Pan, "Quantifying admissible undersampling for sparsity-exploiting iterative image reconstruction in x-ray CT," IEEE Trans. Med. Imaging **32**, 460–473 (2013).
5. Y. Kaganovsky, D. Li, A. Holmgren, H. Jeon, K. P. MacCabe, D. G. Politte, J. A. O'Sullivan, L. Carin, and D. J. Brady, "Compressed sampling strategies for tomography," J. Opt. Soc. Am. A **31**, 1369–1394 (2014).
6. S. S. Hsieh and N. J. Pelc, "The feasibility of a piecewise-linear dynamic bowtie filter," Med. Phys. **40**, 031910 (2013).
7. M. J. Muckley, B. Chen, T. Vahle, T. O'Donnell, F. Knoll, A. D. Sodickson, D. K. Sodickson, and R. Otazo, "Image reconstruction for interrupted-beam x-ray CT on diagnostic clinical scanners," Phys. Med. Biol. **64**, 155007 (2019).
8. T. Lee, C. Lee, J. Baek, and S. Cho, "Moving beam-blocker-based low-dose cone-beam CT," IEEE Trans. Nucl. Sci. **63**, 2540–2549 (2016).
9. N. H. Rezaeian, Y. Xu, B. Li, C. Shen, L. Zhu, and X. Jia, "Experimental development and validation of a rotational blocker concept for under sample CBCT reconstruction and scatter correction in radiation therapy: end to end confirmation," Med. Phys. **46**, E222 (2019).
10. A. P. Cuadros, X. Ma, C. M. Restrepo, and G. R. Arce, "Staticcodect: single coded aperture tensorial x-ray CT," Opt. Express **29**, 20558–20576 (2021).
11. J. Prince and J. Links, Medical Imaging Signals and Systems (Pearson Prentice Hall, 2006).
12. B. Xie, T. Su, V. Kaftandjian, P. Niu, F. Yang, M. Robini, Y. Zhu, and P. Duvauchelle, "Material decomposition in x-ray spectral CT using multiple constraints in image domain," J. Nondestruct. Eval. **38**, 1–9 (2019).
13. A. P. Cuadros, C. M. Restrepo, and P. Noël, "Low-dose dual KVP switching using a static coded aperture," in IEEE 18th International Symposium on Biomedical Imaging (ISBI) (2021), pp. 1057–1061.
14. A. P. Cuadros and G. R. Arce, "Coded aperture optimization in compressive x-ray tomography: a gradient descent approach," Opt. Express **25**, 23833–23849 (2017).
15. A. Parada-Mayorga, A. Cuadros, and G. R. Arce, "Coded aperture design for compressive x-ray tomosynthesis via coherence analysis," in IEEE 14th International Symposium on Biomedical Imaging (ISBI) (2017), pp. 44–47.
16. X.-L. Zhao, W.-H. Xu, T.-X. Jiang, Y. Wang, and M. K. Ng, "Deep plug-and-play prior for low-rank tensor completion," Neurocomputing **400**, 137–149 (2020).
17. A. P. Cuadros, X. Liu, P. E. Parsons, X. Ma, and G. R. Arce, "Experimental demonstration and optimization of x-ray staticcodect," Appl. Opt. **60**, 9543–9552 (2021).
18. W. Xu, F. Xu, M. Jones, B. Keszthelyi, J. Sedat, D. Agard, and K. Mueller, "High-performance iterative electron tomography reconstruction with long-object compensation using graphics processing units (GPUs)," J. Struct. Biol. **171**, 142–153 (2010).
19. J. Hubbell and S. Seltzer, "Radiation and biomolecular physics division, MPL NIST," 2018, https://physics.nist.gov/PhysRefData/XrayMassCoef/tab3.html.
20. J. H. Siewerdsen, A. M. Waese, D. J. Moseley, S. Richard, and D. A. Jaffray, "Spektr: a computational tool for x-ray spectral analysis and imaging system optimization," Med. Phys. **31**, 3057–3067 (2004).
21. T. Rao, G. Arce, and J. Allebach, "Analysis of ordered dither for arbitrary sampling lattices and screen periodicities," IEEE Trans. Acoust. Speech Signal Process. **38**, 1981–2000 (1990).
22. D. L. Lau, R. Ulichney, and G. R. Arce, "Blue and green noise halftoning models," IEEE Signal Process. Mag. **20**(4), 28–38 (2003).
23. A. P. Cuadros, C. Peitsch, H. Arguello, and G. R. Arce, "Coded aperture optimization for compressive x-ray tomosynthesis," Opt. Express **23**, 32788–32802 (2015).
24. A. Cuadros, " Sparse sampling in x-ray computed tomography via spatial and spectral coded illumination," Ph.D. thesis (University of Delaware, 2020).
25. L. Y. Du, J. Umoh, H. N. Nikolov, S. I. Pollmann, T. Y. Lee, and D. W. Holdsworth, "A quality assurance phantom for the performance evaluation of volumetric micro-CT systems," Phys. Med. Biol. **52**, 7087–7108 (2007).
26. Tungsten Heavy Powder and Parts, "Technon poly kits," 2020, https://www.tungstenheavypowder.com/technon-poly-kits/.
27. S. Tilley, W. Zbijewski, and J. W. Stayman, "Model-based material decomposition with a penalized nonlinear least-squares CT reconstruction algorithm," Phys. Med. Biol. **64**, 035005 (2019).
28. G. Arce, "Walnut database," University of Delaware, Department of Electrical & Computer Engineering, 2019, https://www.eecis. udel.edu/~arce/Walnut_Database/.